INSTITUTE OF PHYSICS PUBLISHING and INTERNATIONAL ATOMIC ENERGY AGENCY NUCLEAR FUSION

Nucl. Fusion **47** (2007) 181–188 doi:10.1088/0029-5515/47/3/003

Large density amplification measured on jets ejected from a magnetized plasma gun

Gunsu S. Yun, Setthivoine You and Paul M. Bellan

California Institute of Technology, MC 128-95, Pasadena, CA 91125 USA

E-mail: gunsu@caltech.edu

Received 18 August 2006, accepted for publication 8 January 2007
Published 5 February 2007
Online at stacks.iop.org/NF/47/181

Abstract

Observation of a large density amplification in the collimating plasma jet ejected from a coplanar coaxial plasma gun is reported. The jet velocity is $\sim$30 km s^{-1} and the electron density increases from $\sim 10^{20}$ to 10^{22-23} m^{-3}. In previous spheromak experiments, electron density of the order 10^{19-21} m^{-3} had been measured in the flux conserver region, but no density measurement had been reported for the source gun region. The coplanar geometry of our electrodes permits direct observation of the entire plasma dynamics including the source region. Analysis of Stark broadened spectral lines shows that the electron density increases by a factor of 100 as the jet collimates, with a peak density of up to 10^{22-23} m^{-3}. The observed density amplification is interpreted according to an MHD theory that explains collimation of current-carrying plasma-filled magnetic flux tubes. Issues affecting interpretation of Stark broadened line profiles and the possibility of using the high-density plasma jet for tokamak fuel injection are discussed.

PACS numbers: 95.30.Qd, 52.30.-q, 52.72.+v, 52.70.Kz

(Some figures in this article are in colour only in the electronic version)

1. Introduction

Magnetized coaxial plasma guns are often used to produce plasmas in spheromak formation experiments [1, chapter 7], [2]. The plasma guns have also been used extensively in basic MHD plasma dynamics research [3, 4], injection of plasma into magnetic confinement devices (tokamaks [5–7], mirror machines [8, 9]) simulation of astrophysical phenomena [10] and as thrusters for space propulsion [11]. Because of this wide applicability, there is great interest in measuring and understanding the plasma characteristics (density, temperature, flow velocity, etc) of magnetized coaxial plasma guns. In a typical coaxial plasma gun, neutral gas puffed into a hollow space between two coaxial cylindrical electrodes is ionized, accelerated along the gun axis by MHD forces and ejected from the muzzle, producing a plasma plume. In spheromak experiments, the plasma plume expands into a flux conserver and may relax into a spheromak state. Plasma characteristics in the flux conserver region, a region of much interest, have been well diagnosed and the electron density (n_e) is typically 10^{19-21} m^{-3} [12]. In contrast, little is known about the plasma parameters at the source (i.e. inside the coaxial gun) because of difficulty in accessing that region.

Instead of having a cylindrical geometry, the electrodes of the coaxial plasma gun at Caltech have a coplanar configuration (figure 1(*a*)), permitting direct observation of the entire plasma formation process. This coplanar coaxial gun produces collimated plasma jets of high velocity ($\sim$30 km s^{-1}) and high density ($\sim 10^{22}$ m^{-3}) and has been used to study the physics of spheromaks, MHD instabilities and astrophysical jets [13, 14]. Imaging of the microsecond-scale plasma jet dynamics by a multi-frame high-speed digital camera showed that the jets are axisymmetric, collimated and typically become kink-unstable at a critical length [13]. The images also indicated that the jet velocity is Alfvénic ($\sim$30 km s^{-1}). To rule out the possibility that these camera images result from propagation of either a plasma or an ionization wave rather than an actual flow, a spectroscopic system has been constructed to measure flow velocity from Doppler shifts. The observed Doppler shifts confirmed the Alfvénic speed deduced from the camera images. However, some of the spectral lines showed unexpectedly large broadening, which cannot be explained by the thermal Doppler effect for a credible ion temperature (e.g. $\sim$2 nm for H_β, which would correspond to a Doppler ion temperature of 3000 eV). The only probable cause for such large broadening was attributed to the Stark effect, leading to the conclusion that $n_e \sim 10^{22-23}$ m^{-3}. Initially, this density was considered too high since the jet density was presumed to be of the same order as the plasma density in the flux conserver region reported in previous spheromak experiments. However,

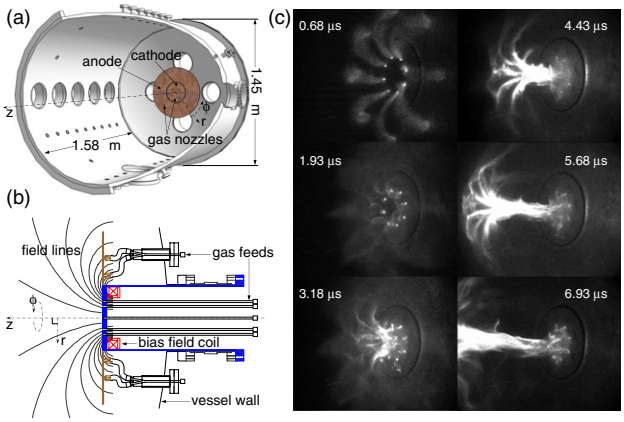

Figure 1. (*a*) Schematic of the vacuum vessel and the coplanar concentric electrodes. A 20.3 cm diameter copper disc (cathode) biased to negative high voltage is surrounded by a 50.8 cm diameter annulus (anode) grounded to the vacuum vessel. The width of the gap between electrodes is 6 mm. (*b*) Side-view schematic of the electrodes showing gas feeds, bias field coil and associated poloidal field lines. (*c*) Typical plasma jet formation sequence (data# 7216, Hydrogen plasma). Eight collimated plasma-filled flux tubes resembling 'spider legs' form along the poloidal field lines linking gas nozzles. They merge to form an axial plasma jet that collimates and expands into the vessel.

the high density measured in the Caltech experiment can be understood by the MHD pumping model that explains why current-carrying magnetized plasmas become collimated [15]; this model shows that plasma is pumped by MHD forces from a wall source into a flux tube and accumulates in the flux tube. The magnetic flux frozen into the ingested plasma also accumulates, increasing the pinch force, and so further increasing the density.

Spectral lines in plasma can experience a broadening via the Stark effect. A concise theoretical overview on Stark broadening can be found in [16, 17] and the physical picture of Stark broadening can be outlined as follows. The quasi-static electric field due to slow moving ions splits a degenerate atomic level of a radiating atom (emitter) into distinct individual components. These split components are then broadened by impacts from fast moving electrons (if the atomic level is not degenerate, the level undergoes only the electron impact broadening). The resulting line profile will be the sum of all possible transitions from the Stark components of an upper level to the Stark components of a lower level. The profile width serves as the first-order description for the Stark broadened line profile although the profile can have many features such as shifts and asymmetries. The profile width has a strong dependence on charged particle density (especially electron density) and so Stark broadening provides a convenient and inexpensive method for determining plasma density [18]. Theories that take into account additional effects such as Debye screening [19] and ion dynamics [20–22] have predicted Stark broadening of hydrogen Balmer lines in good agreement with experiments. Measurements of Stark broadening of non-hydrogenic spectral lines have also been tabulated for well-defined and independently measured plasma conditions [23, 24].

Hydrogen Balmer lines have been the most popular choice for plasma density diagnosis because of well-established theoretical and experimental studies on Balmer lines and their strong Stark effect. In particular, the H_β line is the best density indicator because its Stark width is nearly independent of plasma temperature. When H_β Stark broadening is small compared with other broadening effects such as Doppler broadening and Zeeman splitting, higher-n Balmer lines can be used since the Stark broadening is generally larger for higher principal quantum number n. For example, merging of high-n Balmer lines (i.e. Inglis–Teller limit) has been utilized to determine the density in edge regions ($n_e \sim 10^{20\text{–}21}\,\mathrm{m}^{-3}$, $B \sim$ several Teslas) of tokamak devices [22, 25, 26]. Our experiment lies in the opposite situation, namely where H_β Stark broadening is large compared with Zeeman and Doppler effects.

We report here density measurements using Stark broadened profiles of visible emission lines from the Caltech spheromak formation/astrophysical jet simulation experiment. The measurements clearly demonstrate a large density amplification (increase from $\sim 10^{20}$ to $10^{22\text{–}23}\,\mathrm{m}^{-3}$) associated with collimation of the plasma jet, as explained by the MHD pumping theory. The possibility of injecting a high-density plasma jet into a magnetized plasma of fusion interest and the issues affecting the interpretation of Stark broadened line profiles are also discussed.

2. Experimental setup

The setup of the Caltech spheromak experiment is shown schematically in figures 1(*a*) and (*b*) and the typical plasma jet formation sequence is shown in figure 1(*c*). The geometry of the experiment is characterized by a cylindrical coordinate system $\{r, \phi, z\}$, where z is the direction along the axis of symmetry, ϕ is the azimuthal direction about the axis and r is the radial distance from the axis. The r, z directions will be called the poloidal direction and the ϕ direction will be called the toroidal direction. The details of the experiment can be found elsewhere [13, 14] and will be summarized here. The spheromak gun has a disc cathode surrounded by a coaxial, coplanar annulus anode (figure 1(*a*)). Each electrode has eight gas nozzles regularly placed in a circle around the axis of symmetry. A poloidal magnetic field (B_r, B_z) is generated by a coil located behind the cathode (figure 1(*b*)). Neutral gas is puffed through the nozzles into the vacuum vessel ($\sim 10^{-7}$ Torr base pressure), and the gas breaks down when high voltage ($\sim$5 kV) is applied between the electrodes. Eight plasma-filled magnetic flux tubes resembling spider legs are then formed along the poloidal field lines (figure 1(*c*)). Each tube connects a nozzle on the cathode and its corresponding nozzle on the anode and carries an electric current of $\sim$10 kA. Later, the eight tubes merge to form an axial plasma jet (figure 1(*c*)). The plasma jets have the following nominal parameters: electron density $n_e \sim 10^{20\text{–}23}\,\mathrm{m}^{-3}$ (to be discussed), velocity $U_z \sim$ 10–50 km s^{-1}, electron and ion temperatures $T_e \simeq T_i \sim$ 1–5 eV, magnetic field strength $B \sim$ 0.01–0.3 T, electric current $I_0 \sim$ 80 kA, axial length $\sim$25 cm and diameter $\sim$5 cm.

The spectroscopic system shown schematically in figure 2 has been developed to measure emission spectra from the plasma jets. This system is triggered at plasma breakdown as determined by the sudden change in the gun voltage (indicated bold vertical line in figure 2(f)). The trigger jitter is about

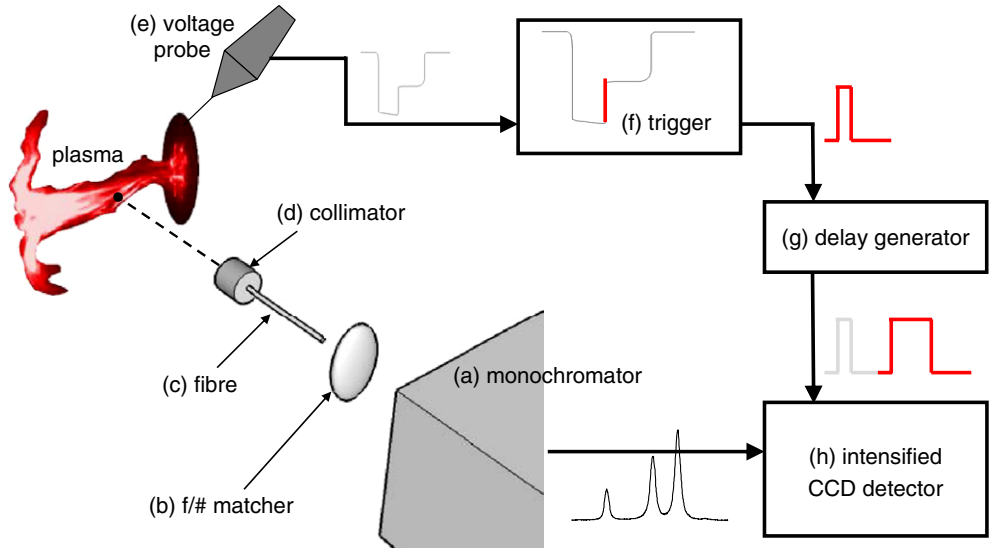

Figure 2. Schematic drawing of the spectroscopic system. The system consists of (a) Czerny-Turner monochromator (JY Horiba 1000M: focal length = 1 m, f/# = f/8, grating density = 3600 grooves mm^{-1}, wavelength range = 200–500 nm), (b) f/# matching optics (c) optical fibre (Ocean Optics QP200-2-UV-VIS: 10 meter long, core diameter = 200 μm, NA = 0.22), (d) collimator (Ocean Optics 74UV: lens diameter = 5 mm, focal length = 10 mm), (e) high-voltage probe to trace the gun voltage, (f) trigger to generate a pulse at plasma breakdown (g) delay generator (BNC 555) to generate a gate signal and (h) intensified CCD detector (Andor ICCD DH520: 1024 × 256 pixels, 800 × 256 active pixels).

0.1 μs due to the finite rise time of the voltage. The trigger signal goes to a delay generator (figure 2(g)) which sends a pulse to gate the intensified CCD (ICCD) camera (figure 2(h)).

The spectral resolution of the spectroscopic system is calculated from the monochromator and ICCD parameters according to

$$R(\lambda) = \frac{\Delta x}{2L}\left(\sqrt{\left(\frac{2d\cos\alpha_0}{m}\right)^2 - \lambda^2} + \lambda\tan\alpha_0\right), \qquad (1)$$

where $R(\lambda)$ is the resolution per ICCD pixel, Δx is the pixel size, L is the focal length of the monochromator, α_0 is half the angle between the incident and the diffracted light on the grating, d is the groove spacing of the grating, m is the diffraction order and λ is the selected wavelength. The derivation of equation (1) is given in the appendix. The accuracy of this calculation has been verified over a wide range of reference wavelengths using spectral lamps (Hg, D_2, O_2 and Ar). The typical spectral resolution and band-pass are ∼5 pm/pixel and ∼4 nm respectively. The temporal resolution, i.e. minimum gate width of the ICCD detector with reasonable signal-to-noise ratio, is about 0.3 μs. The temporal resolution is mainly limited by optical throughput, which is maximized by matching f-numbers between optical components. The spatial resolution is determined by sending a HeNe laser beam backward through the fibre and observing the size of the red spot this laser beam makes on an electrode. The observed HeNe spot size is approximately 10 mm. The spatial resolution is also affected by the temporal resolution because the plasma jets move very fast. For example, if the ICCD gate width is 1 μs and the jet velocity is 30 km s^{-1}, the detector signal is integrated over the jet travel distance of 3 cm.

In the experiments reported here, highly repeatable straight (neither kinked nor detached) plasma jets of single species (hydrogen or nitrogen) are generated. A set of emission spectra are taken for a fixed wavelength by varying the gate timing over the plasma lifetime. The line-of-sight is varied to probe the plasma jet along its axis as shown in figure 3.

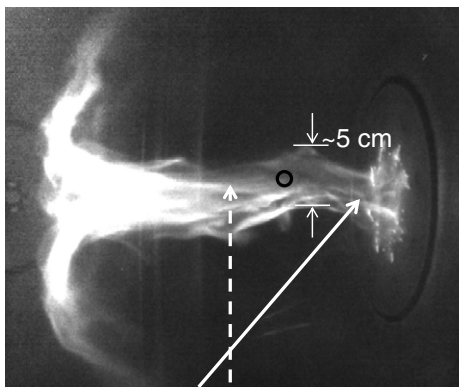

Figure 3. Line-of-sight of the spectroscopic system is varied to probe the plasma along its axis. The dashed line is perpendicular to the axis of the plasma and the solid line is off-axis toward the electrode. The circle represents the size of the line-of-sight (∼10 mm in diameter).

3. Density estimation from spectral line profiles

For the purpose of electron density measurement, Stark broadening is often approximated by a Lorentzian profile characterized by its full width at half maximum (FWHM). For many spectral lines, the electron density is a simple function of the Stark FWHM. However, extraction of Stark widths from spectral line profiles is generally not straightforward. To clarify difficulties in reliable density estimation from the Stark broadened line profiles, issues pertinent to our plasma source are now discussed [18].

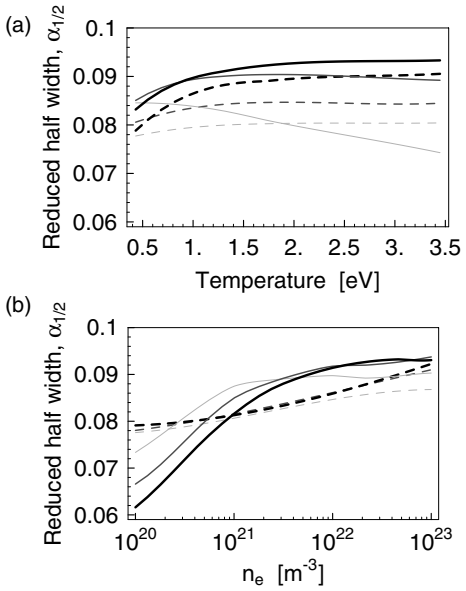

Figure 4. Reduced half width $\alpha_{1/2}$ of theoretical H_β Stark profiles according to the GC theory (solid lines) and according to the KG theory (dashed lines). (a) $\alpha_{1/2}$ versus temperature for densities 5×10^{20}, 5×10^{21}, 5×10^{22} m^{-3}. The higher the density, the thicker and bolder the line is rendered. (b) $\alpha_{1/2}$ versus density for temperatures 1, 2 and 3 eV. The higher the temperature, the thicker and bolder the line is rendered.

3.1. Uncertainty in Stark parameter

For hydrogen lines, electron density is related to the Stark width by the relation

$$w_S = 2.5 \times 10^{-14}\, \alpha_{1/2}\, n_e^{2/3}, \qquad (2)$$

where w_S is the Stark FWHM in nm, n_e is the electron density in m^{-3} and $\alpha_{1/2}$ is the so-called reduced *half*-width that scales the line shape [18]. The half-width $\alpha_{1/2}$ has been tabulated for many hydrogen lines based on both theoretical calculations and experimental data for the temperature range 0.5–4 eV and density range $10^{20\text{–}24}$ m^{-3} [19, 20, 22]. The half-width $\alpha_{1/2}$ has a weak dependence on density and on temperature. In addition, it differs slightly between calculations. The half-width $\alpha_{1/2}$ of the H_β line (approximately 0.085) is plotted as a function of temperature (density) for several representative densities (temperatures) in figures 4(*a*) and (*b*) according to the Gigosos–Cardeñoso (GC) theory [20] and according to the Kepple–Griem (KG) theory [19], showing a slight discrepancy between the two theories. The uncertainty in $\alpha_{1/2}$ introduces an error <20% in density estimation for our hydrogen plasma jets.

For lines of non-hydrogenic neutral and singly ionized atoms, the theoretical Stark broadening is to a first approximation linearly proportional to the electron density [18]:

$$w_S \approx w_m n_e, \qquad (3)$$

where w_m is the proportionality parameter. For an extensive collection of N II lines, this property has been substantiated by the experimental work of Mar *et al* [24]. The N II line at 424.178 nm ($w_m = 0.1526\,\text{nm}/10^{23}\,m^{-3}$) is used to measure the density of nitrogen plasma jets in our experiment. The uncertainty of the parameter w_m for this line is <23% [23].

3.2. Competing broadening effects

Besides Stark broadening, a spectral line can be broadened by other effects such as Doppler effect, instrumental broadening and Zeeman splitting.

The Doppler broadening due to the thermal motion of emitters is a Gaussian function with FWHM $w_D = 7.7 \times 10^{-5}\lambda\sqrt{T_i/M}$, where λ is the wavelength in nm, T_i is the ion temperature in eV and M is the ion mass in amu. For $\lambda = 300$–500 nm and $T_i = 1$–10 eV, the Doppler width w_D is 0.02–0.1 nm for hydrogen and 0.006–0.03 nm for nitrogen. The presumption of low-ion temperature $T_i \leqslant 10$ eV in our plasma is supported by an impurity line measurement (C III 229.687 nm) showing broadening $\leqslant 0.01$ nm corresponding to $T_i \leqslant 4$ eV (see the inset profile in figure 7). It had been assumed that $T_i \sim T_e$ in our previous work [13, 14], where T_e was either measured by a triple Langmuir probe (5–15 eV) or inferred from spectral line ratios (1–5 eV). For nitrogen plasma jets, the assumption was supported by a good agreement between measured line ratios and calculated line ratios using the Saha–Boltzman equation, suggesting that our plasma jet is at local thermodynamic equilibrium and so $T_i \sim T_e$. Significant ion heating ($T_i \gg T_e$) via magnetic reconnection has been observed in some other gun-produced spheromak plasmas [1, chapter 13]. However, magnetic reconnection is not a dominant mechanism in the plasma jet under consideration here as the magnetic topology is not undergoing changes. There is mainly a stretching of field lines, but not reconnection (except for the minimal reconnection associated with merging of spider legs).

The instrumental broadening is ~7 pixels on the ICCD detector corresponding to ~0.03 nm. The Zeeman splitting ($\sim 10^{-7}\lambda^2 B < 0.008$ nm for $B = 0.3$ T) is negligible. Spectral lines can also split due to Doppler shifts if there exist relative bulk flow motions within the line-of-sight volume. However, such a splitting will be minimal because it is less than 0.05 nm even for unlikely 30 km s^{-1} relative flow motions.

For a H_β line width > 0.2 nm, Stark effect must be the dominant broadening effect because the other effects cannot account for a line width > 0.1 nm. In terms of electron density, Stark effect will be the dominant broadening of the H_β line for $n_e > 10^{21}$ m^{-3}.

3.3. Plasma inhomogeneity

The plasma jets in our experiments have internal structures (see figure 3) and so may have a density gradient along the line-of-sight. A significant distortion may occur at the centre of a line profile as illustrated in figure 5(*a*) because the lower density region concentrates its emission energy in a narrow band while the higher density region spreads the emission energy over a broad band.

In particular, special care must be applied to the interpretation of the characteristic central dip of the H_β line. The density gradient effect becomes more appreciable in the central dip region as the narrow H_β emission from the low-density region can stand out in that region. The H_β central dip can appear in high-density plasma, where the ion field discussed in section 1 is strong enough to make the line splitting (via the linear Stark effect [27]) larger than the electron impact broadening. The other even-numbered hydrogen Balmer lines

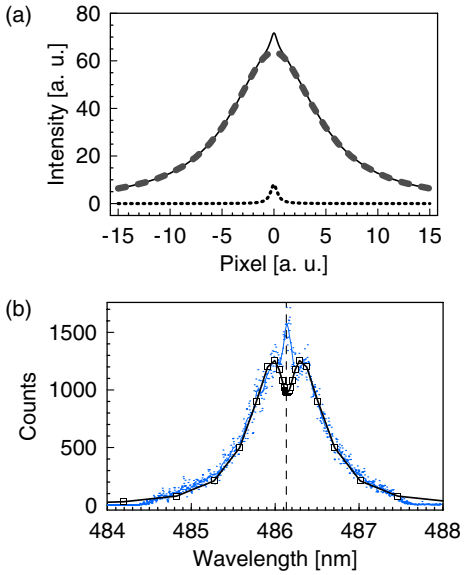

Figure 5. (*a*) Sum of a wide and a narrow Lorentzian profile. Dashed line is the wide profile with total intensity = 1000 and FWHM = 10, dotted line is the narrow profile with total intensity = 20 and FWHM = 0.5 and solid line is the sum of the two profiles. (*b*) Measured H_β line profile showing the characteristic central dip distorted by a peak from a low-density contribution (data# oma11.61, perpendicular line-of-sight). Measured data points are represented by dots with a fitting curve (thin solid line). Bold solid line connecting the square points is a theoretical fit according to Stehlé [22] with $n_e = 1.05 \times 10^{22}\,m^{-3}$ and $T = 2\,eV$. The profile calculation by Stehlé is for a pure hydrogen plasma at local thermodynamic equilibrium [21] and so $T_i = T_e$. Vertical dashed line indicates the H_β rest-frame wavelength 486.133 nm.

can also have a central dip [26]. Non-hydrogenic lines cannot have such a central dip because their line splittings (occurring via the quadratic Stark effect [27]) are small.

A narrow peak overlaid over a broad envelope similar to figure 5(*a*) was indeed observed in some measured H_β line profiles (figure 5(*b*)). Note that the theoretical fit according to Stehlé [22] lacks such a narrow peak because the theory assumes a homogeneous plasma density. The electron density may be underestimated if the peak value is used to measure the profile FWHM. In our analysis, the FWHM is obtained by fitting the profile to a Lorentzian shape, since this fitting process puts more weight on the side bands than on the centre and so avoids errors associated with density gradient along the line-of-sight.

3.4. Self-absorption, continuum background and blending with nearby spectral lines

Self-absorption in an optically thick plasma can lead to an overestimation of electron density. Overlaps between the internal structure of the plasma jet and the objects in the background are observed in camera images when the camera is operated within its dynamic range, i.e. not saturated (see figure 3). This suggests that our plasma is optically thin and so self-absorption will be insignificant.

Blackbody radiation, the background noise of the ICCD detector, Balmer continuum, etc all contribute to the background level of spectral data. Spectral profiles are

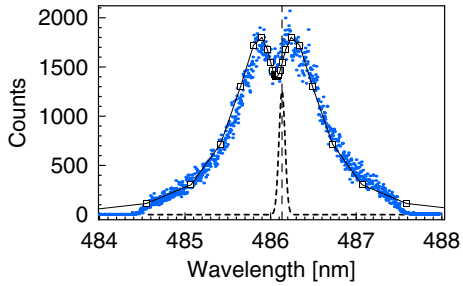

Figure 6. H_β profile with the characteristic central dip (data# oma11.28). The square points are the theoretical Stark profile for $n_e = 1.3 \times 10^{22}\,m^{-3}$ and $T = 2\,eV$ by Stehlé [22]. A Doppler profile (dashed line) for $T_i = 5\,eV$ at $\lambda = 486.133$ nm (H_β) is also shown for comparison with the much broader Stark profile. The estimated Stark FWHM according to equation (4) is ∼1.1 nm, corresponding to $n_e \sim 1.2 \times 10^{22}\,m^{-3}$. Note that the data points near the profile tail ends are flat since they are outside the band-pass of the spectroscopic system.

corrected by subtracting the measured background level taken from spectral regions close to the spectral line of interest but separated by several times its width. Additionally, every spectral line chosen in our experiment is isolated from other lines by at least several times its width to avoid mixing with nearby spectral lines.

4. Experimental observation

The total FWHM (w_T) of a spectral line profile is measured by fitting the data to a Lorentzian profile. The Stark FWHM (w_S) is obtained by subtracting the Doppler effect (w_D) and the instrumental broadening (w_I) according to the conventional method [28]

$$w_S = \sqrt{w_T^2 - w_D^2 - w_I^2} \qquad \text{if } w_T/\sqrt{w_D^2 + w_I^2} > 1.04, \quad (4)$$

or according to the empirical Voigt profile approximation [29] otherwise. The electron density is then calculated using equation (2) for hydrogen lines or equation (3) for non-hydrogenic lines. The reliability of this simple and computationally inexpensive method is substantiated by comparing the density obtained by this method with the density obtained by the theoretical fitting according to Stehlé [22] (see figure 6). The error in the density estimation using H_β profiles is 50% for $10^{20}\,m^{-3}$, 25% for $10^{21}\,m^{-3}$ and 15% for $10^{22}\,m^{-3}$, taking into account issues discussed in section 3.

The H_β and H_γ line profiles from hydrogen plasmas show very large broadenings (>1 nm) indicative of a strong Stark effect. The central dip in the H_β profile as shown in figure 6 also suggests a strong Stark effect [18]. The nitrogen line profiles from nitrogen plasmas also show large Stark broadenings and typical data are shown in figure 7.

The time dependence of the electron density obtained from Stark broadening measurement is plotted in figure 8. A very high density of the order $10^{22}\,m^{-3}$ is observed when the central column of jet is fully formed. The density is $\sim 10^{20}\,m^{-3}$ when the plasma starts to form the central jet and increases by a factor of 100 when the jet fully forms. This is consistent with the magnetic flux tube becoming filled with plasma by the ingestion/collimation process discussed in the

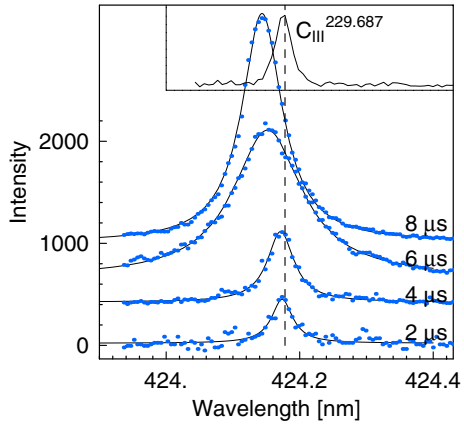

Figure 7. Observed line profiles (N II, 424.178 nm) from a nitrogen plasma jet at $t = 2$, 4, 6 and 8 μs after breakdown (data#: 6736–3, 7, 11 and 15, respectively). Solid lines are Lorentzian fits. The estimated densities are 0.1, 1.7, 7.8 and 4.0×10^{22} m^{-3} respectively. A measured impurity profile (C III, 229.687 nm) is inset at the top for width comparison. Its Doppler width ($w_{\rm D} = \sqrt{w_{\rm T}^2 - w_{\rm I}^2}$) is ~0.007 nm, corresponding to $T_{\rm i} = 2$ eV. Vertical dashed line indicates rest-frame wavelength.

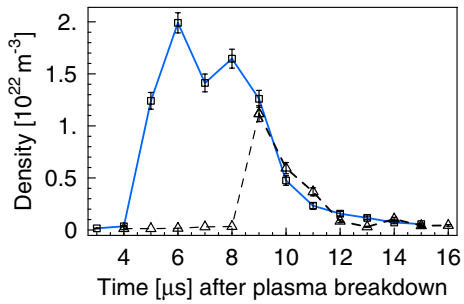

Figure 8. Time dependence of hydrogen plasma electron density (from data# oma11.16~69). Squares correspond to the solid (oblique) line-of-sight and triangles to the dashed (perpendicular) line-of-sight in figure 3. For the perpendicular line-of-sight, the density is zero initially and appears suddenly at $t = 9$ μs as expected because the jet takes time to reach the line-of-sight volume. This is consistent with the jet velocity 10 cm/3 μs ≈ 30 km s^{-1}.

MHD pumping theory [15]. Nitrogen plasmas show similar time dependence of electron density but have even greater peak density $\sim 1 \times 10^{23}$ m^{-3}.

5. Discussion and conclusions

The Stark broadening density measurement shows that the plasma jets become very dense on a microsecond time scale. This result is supported by an independent density measurement from a laser interferometer [30]. The density of the pre-breakdown neutral gas, as measured by a fast ion gauge, is only 10^{17} m^{-3} [14]. The measured peak plasma jet density is of the order 10^{22} m^{-3} at the same location 6 μs later, so the particle density has increased by a factor of 10^5. This steep density rise cannot be explained by a pinch effect associated with the current flowing in the jet flux tube. Particles must be pumped into the flux tube from the source gas nozzles.

According to the MHD pumping model [15], the driving force of the plasma jet dynamics is the axial gradient of the toroidal magnetic energy associated with the axial current:

$$\rho\frac{{\rm d}U_z}{{\rm d}t} = (\boldsymbol{J}\times\boldsymbol{B})_z - \frac{\partial P}{\partial z} = J_r B_\phi - J_\phi B_r - \frac{\partial P}{\partial z}$$
$$= -\frac{\partial}{\partial z}\left(\frac{B_\phi^2}{2\mu_0}\right) - \frac{\partial P}{\partial z} - J_\phi B_r \approx -\frac{\partial}{\partial z}\left(\frac{B_{\phi,a}^2}{\mu_0}\right) - J_\phi B_{\rm r}, \tag{5}$$

where U_z is the z-directed jet velocity, ρ is the mass density, B is the magnetic field, J is the current density, P is the pressure and a denotes the flux tube radius. $B_{\phi,a}$ is the toroidal magnetic field at $r = a$ and the term $J_\phi B_r$ is very small initially. Note that the pressure term and the magnetic energy term are incorporated into a single effective potential term $B_{\phi,a}^2/\mu_0$ in the last step by assuming radial pressure balance [15, section III(B)]. The potential has negative slope everywhere because $B_{\phi,a}$ decreases along the axis due to the flared geometry of the jet flux tube. Thus, the jet will fall down the slope and gain kinetic energy as it moves. The order of magnitude of the jet kinetic energy will be

$$\rho U_z^2 \approx -\Delta\left(\frac{B_{\phi,a}^2}{\mu_0}\right) \approx \left(\frac{B_{\phi,a}^2}{\mu_0}\right)_{z=0}. \tag{6}$$

Using $\rho = m_{\rm i} n_{\rm e}$, $n_{\rm e} \approx \left(B_{\phi,a}^2/\mu_0\right)_{z=0}/m_{\rm i}U_z^2$, where $m_{\rm i}$ is the ion mass. The observed $U_z \sim 30$ km s^{-1} and $B_{\phi,a} \sim 0.1$ T give electron density $n_{\rm e}$ of the order 10^{22} m^{-3}, which is consistent with the Stark broadening density measurement. However, the observed density amplification cannot be explained by this consistency check alone.

Density can build up if there exists a negative axial velocity gradient ($\partial U_z/\partial z < 0$) according to the continuity equation:

$$\frac{{\rm d}\rho}{{\rm d}t} = -\rho\nabla\cdot\boldsymbol{U} = -\rho\frac{\partial U_z}{\partial z} - \rho\nabla_\perp\cdot\boldsymbol{U}_\perp \tag{7}$$

where negative $\partial U_z/\partial z$ represents an axial compression and negative $\nabla_\perp\cdot\boldsymbol{U}_\perp$ represents a radial compression (pinch). In case of dominant axial compression (i.e. $\partial U_z/\partial z \ll 0$), it can be easily seen that density increases since ${\rm d}\rho/{\rm d}t \approx -\rho\partial U_z/\partial z > 0$. Flow deceleration (${\rm d}U_z/{\rm d}t < 0$) is also linked to a large axial compression since ${\rm d}U_z/{\rm d}t = \partial U_z/\partial t + U_z\partial U_z/\partial z \approx U_z\partial U_z/\partial z < 0$.

Slowing down of the jet (${\rm d}U_z/{\rm d}t < 0$) at the flow front has been observed in camera images and Doppler shift measurements. The cause of the flow deceleration has not yet been investigated but could be the tension of the curved poloidal field lines or buildup of neutral particles swept by the jet at the flow front. The jet deceleration results in accumulation of mass (${\rm d}\rho/{\rm d}t > 0$) and accumulation of the toroidal magnetic flux carried by the mass flow. As the magnetic flux accumulates, the magnetic field intensity increases and so does the pinch force. The amplified pinch force subsequently squeezes the plasma ($\nabla_\perp\cdot\boldsymbol{U}_\perp < 0$), further increasing particle density and collimating the flow. This collimation scenario has been verified quantitatively for the spider legs in the previous study [14]. The same pumping/deceleration/collimation theory accounts for the observed density amplification of the magnetized current-carrying plasma jet.

Recent work by Voronin *et al* [7] suggests that our coplanar plasma gun producing high-density plasma jets by the MHD pumping mechanism might be capable of fuelling a magnetized plasma of fusion interest. In the Voronin *et al* experiment, high-kinetic energy plasma jets were produced by a double-stage Marshall gun which first ionizes a hydrogen gas released from titanium grains and then accelerates the resulting hydrogen plasma. These plasma jets were successfully injected into the Globus-M spherical tokamak and had parameters comparable to our experiment (Globus-M: $n_e \sim 10^{22}\,\mathrm{m}^{-3}$, total number of accelerated particles $N_{tot} \sim 1\text{–}5 \times 10^{19}$, $U_z \sim 50\text{–}100\,\mathrm{km\,s}^{-1}$, and our experiment: $n_e \sim 10^{22\text{–}23}\,\mathrm{m}^{-3}$, $N_{tot} \sim 10^{19}$, $U_z \sim 30\,\mathrm{km\,s}^{-1}$). This suggests that our plasma jets may be suitable for tokamak fuelling. Higher velocity for deep penetration [1, chapter 16] can be achieved by increasing the gun current and the minimal contact with electrodes in our plasma gun ensures purity of the plasma jets.

Acknowledgment

This work was supported by US DoE Grant DE-FG02-04ER54755.

Appendix A. Appendix. Linear dispersion of Czerny–Turner monochromator

A Czerny–Turner monochromator is shown schematically in figure A1. Knowledge of the linear dispersion of the monochromator at the exit plane is desired to calibrate a spectral window for which no reference spectral lamps are available and also to circumvent repetitive use of spectral lamps for each spectral window. The grating equation is

$$d\,(\sin\alpha + \sin\beta) = m\lambda, \tag{A.1}$$

where α is the angle of incidence, β is the angle of diffraction, d is the groove spacing, m is the diffraction order and λ is the wavelength of light. The sign of an angle is positive (negative) if drawn counterclockwise (clockwise) in figure A1. The angular dispersion at the focusing mirror ($M2$) is obtained by differentiating equation (A.1) with respect to λ:

$$d\cos\beta\frac{\partial\beta}{\partial\lambda} = m \Longrightarrow \frac{\partial\beta}{\partial\lambda} = \frac{m}{d\cos\beta}. \tag{A.2}$$

Thus, the linear dispersion at the exit focal plane is

$$\frac{\partial\lambda}{\partial x} = \frac{1}{L}\frac{\partial\lambda}{\partial\beta} = \frac{d\cos\beta}{Lm}, \tag{A.3}$$

where L is the focal length of the focusing mirror.

A rotation of the grating by an angle θ determines the incidence/diffraction angles and selects a wavelength λ according to equation (A.1):

$$\alpha = \alpha_0 + \theta; \qquad \beta = -\alpha_0 + \theta \tag{A.4}$$

$$d\,(\sin(\alpha_0+\theta) + \sin(-\alpha_0+\theta)) = 2d\sin\theta\cos\alpha_0 = m\lambda$$
$$\Longrightarrow \sin\theta = \frac{m\lambda}{2d\cos\alpha_0}. \tag{A.5}$$

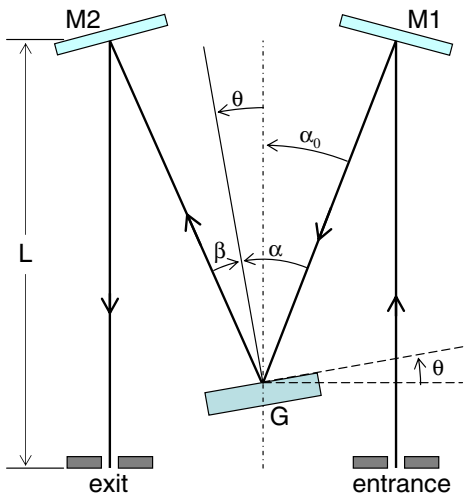

Figure A1. Czerny–Turner configuration. G is the grating with groove spacing d. $M1$ is the collimating mirror and $M2$ is the focusing mirror with focal length L. α is the angle of incidence, β is the angle of diffraction, α_0 is half the angle between the incident and the diffracted light and θ is the rotation angle of the grating.

The linear dispersion can be expressed as a function of the selected wavelength by inserting equations (A.4) and (A.5) in equation (A.3):

$$\frac{\partial\lambda}{\partial x} = \frac{d}{Lm}\cos(-\alpha_0+\theta) = \frac{d}{Lm}\,(\cos\alpha_0\cos\theta + \sin\alpha_0\sin\theta)$$
$$= \frac{d}{Lm}\left(\cos\alpha_0\frac{\sqrt{(2d\cos\alpha_0)^2 - (m\lambda)^2}}{2d\cos\alpha_0} + \sin\alpha_0\frac{m\lambda}{2d\cos\alpha_0}\right)$$
$$= \frac{1}{2L}\left(\sqrt{\left(\frac{2d\cos\alpha_0}{m}\right)^2 - \lambda^2} + \lambda\tan\alpha_0\right) \tag{A.6}$$

The pixel resolution $R(\lambda)$ of a CCD detector placed at the exit focal plane is $R(\lambda) = \Delta x\,\partial\lambda/\partial x$, where Δx is the detector pixel size.

References

[1] Bellan P.M. 2000 *Spheromaks* (London: Imperial College Press)
[2] Jarboe T.R. 1994 Review of spheromak research *Plasma Phys. Control. Fusion* **36** 945–90
[3] Alfvén H., Lindberg L. and Mitlid P. 1960 Experiments with plasma rings *J. Nucl. Energy* C **1** 116–20
[4] Marshall J. and Stratton T.F. 1962 The collision of two plasmas *Nucl. Fusion Suppl.* **2** 663–74
[5] Leonard A.W, Dexter R.N. and Sprott J.C. 1986 Trapping of gun-injected plasma by a tokamak *Phys. Rev. Lett.* **57** 333–6
[6] Brown M.R. and Bellan P.M. 1992 Efficiency and scaling of current drive and refuelling by spheromak injection into a tokamak *Nucl. Fusion* **32** 1125–37
[7] Voronin A.V., Gusev V.K., Yu V. Petrov, Sakharov N.V., Abramova K.B., Sklyarova E.M. and S. Yu. Tolstyakov 2005 High kinetic energy plasma jet generation and its injection into the Globus-M spherical tokamak *Nucl. Fusion* **45** 1039–45
[8] Francis G., Mason D.W. and Hill J.W. 1964 Containment of plasma in a magnetic mirror, with hexapole stabilizing fields *Nature* **203** 623–4

[9] Swanson D.G., Clark R.W., Korn P., Robertson S. and Wharton C.B. 1972 rf plasma heating in a mirror machine at frequencies near the ion cyclotron frequency and its harmonics *Phys. Rev. Lett.* **28** 1015–9
[10] Bellan P.M. 2005 Miniconference on astrophysical jets *Phys. Plasmas* **12** 058301
[11] Burton R.L. and Turchi P.J. 1998 Pulsed plasma thruster *J. Propul. Power* **14** 716–35
[12] Bruhns H. 1986 Recent compact toroid research *Plasma Phys. Control. Fusion* **28** 1389–400
[13] Hsu S.C. and Bellan P.M. 2003 Experimental identification of the kink instability as a poloidal flux amplification mechanism for coaxial gun spheromak formation *Phys. Rev. Lett.* **90** 215002
[14] You S., Yun G.S. and Bellan P.M. 2005 Dynamic and stagnating plasma flow leading to magnetic-flux-tube collimation *Phys. Rev. Lett.* **95** 045002
[15] Bellan P.M. 2003 Why current-carrying magnetic flux tubes gobble up plasma and become thin as a result *Phys. Plasmas* **10** 1999–2008
[16] Lisitsa V.S. 1977 Stark broadening of hydrogen lines in plasmas *Sov. Phys. Usp.* **20** 603–30
[17] Luque J.M., Calzada M.D. and Sáez M. 2003 Experimental research into the influence of ion dynamics when measuring the electron density from the Stark broadening of the H_α and H_β lines *J. Phys. B: At. Mol. Opt. Phys.* **36** 1573–84
[18] Wiese W.L. 1965 *Plasma Diagnostic Techniques* (New York: Academic)
[19] Kepple P. and Griem H.R. 1968 Improved Stark profile calculations for the hydrogen lines H_α, H_β, H_γ, and H_δ *Phys. Rev.* **173** 317–25
[20] Gigosos M.A. and Cardeñoso V. 1996 New plasma diagnosis tables of hydrogen Stark broadening including ion dynamics *J. Phys. B: At. Mol. Opt. Phys.* **29** 4795–838
[21] Stehlé C. 1994 Stark broadening of hydrogen Lyman and Balmer in the conditions of stellar envelopes *Astron. Astrophys. Suppl. Ser.* **104** 509–27
[22] Stehlé C. and Hutcheon R. 1999 Extensive tabulations of Stark broadened hydrogen line profiles *Astron. Astrophys. Suppl. Ser.* **140** 93–7
[23] Konjević N., Lesage A., Fuhr J.R. and Wiese W.L. 2002 Experimental Stark widths and shifts for spectral lines of neutral and ionized atoms *J. Phys. Chem. Ref. Data* **31** 819–927
[24] Mar S., Aparicio J.A., de la Rosa M.I., del Val J.A., Gigosos M.A., González V.R. and Pérez C. 2000 Measurement of Stark broadening and shift of visible N II lines *J. Phys. B: At. Mol. Opt. Phys.* **33** 1169–84
[25] Marandet Y., Genesio P., Koubiti M., Godbert-Mouret L., Felts B., Stamm R., Capes H. and Guirlet R. 2004 Characterization of tokamak edge plasmas using spectroscopic line profiles *Nucl. Fusion***44** 118–22
[26] Welch B.L., Griem H.R., Terry J., Kurz C., LaBombard B., Lipschultz B., Marmar E. and McCracken G. 1995 Density measurements in the edge, divertor and X-point regions of Alcator C-Mod from Balmer series emission *Phys. Plasmas* **2** 4246–51
[27] Landau L.D. and Lifshitz E.M. 2002 *Quantum Mechanics: Non-Relativistic Theory* 3rd edn (Oxford: Butterworth–Heinemann)
[28] Mimura M. and Sato K. 1995 Convolution-fitting method for Doppler-broadening plasma ion temperature measurement *Japan. J. Appl. Phys.* **34** 1668–72
[29] Liu Y., Lin J., Huang G., Guo Y. and Duan C. 2001 Simple empirical analytical approximation to the Voigt profile *J. Opt. Soc. Am.* B **18** 666–72
[30] Kumar D. and Bellan P.M. 2006 Heterodyne interferometer with unequal path lengths *Rev. Sci. Instrum.* **77** 083503